In Vivo Three-Dimensional Raster Scan Optoacoustic Mesoscopy Using Frequency Domain Inversion

Qutaiba Mustafa, Murad Omar, Ludwig Prade, Pouyan Mohajerani, Antonios Stylogiannis, Vasilis Ntziachristos, *Fellow, IEEE*, and Christian Zakian

***Abstract*— Optoacoustic signals are typically reconstructed into images using inversion algorithms applied in the time-domain. However, time-domain reconstructions can be computationally intensive and therefore slow when large amounts of raw data are collected from an optoacoustic scan. Here we considered a fast weighted $\omega - k$ (FWOK) algorithm operating in the frequency domain to accelerate the inversion in raster-scan optoacoustic mesoscopy (RSOM), while seamlessly incorporating impulse response correction with minimum computational burden. We investigated the FWOK performance with RSOM measurements from phantoms and mice *in vivo* and obtained 360-fold speed improvement over inversions based on the back-projection algorithm in the time-domain. This previously unexplored inversion of *in vivo* optoacoustic data with impulse response correction in frequency domain reconstructions points to a promising strategy of accelerating optoacoustic imaging computations, toward video-rate tomography.**

***Index Terms*— Fast Fourier transform, Omega-k migration, transfer function, optoacoustics, photoacoustics, mesoscopy.**

Abbreviations

FWOK	Fast Weighted Omega K.
TD	Time-Domain.
FD	Frequency Domain.
RSOM	Raster Scan Optoacoustic Mesoscopy.
MIP	Maximum intensity Projection.
FFT	Fast Fourier Transform.
SNR	Signal-to-noise Ratio.
STF	Spatial Transfer Function.

Manuscript received April 13, 2021; accepted May 23, 2021. Date of publication May 27, 2021; date of current version November 30, 2021. This work was supported in part by the Deutsche Forschungsgemeinschaft (DFG) through the Sonderforschungsbereich (SFB)/Transregio 179 (TP13) and CRC 1123 (Z1) Projects and in part by the Bundesministerium für Bildung und Forschung (BMBF), Bonn, Germany, through the Project Sense4Life, under Grant 13N13855. The work of Christian Zakian was supported by the European Union's Horizon 2020 Research and Innovation Program through the Hybrid optical and optoacoustic endoscope for esophageal tracking (ESOTRAC) Project under Grant 732720. *(Corresponding author: Christian Zakian.)*

This work involved human subjects or animals in its research. Approval of all ethical and experimental procedures and protocols was granted by the Government of Upper Bavaria.

The authors are with the School of Medicine, Chair of Biological Imaging, Central Institute for Translational Cancer Research (TranslaTUM), Technical University of Munich, 81675 Munich, Germany, and also with the Institute of Biological and Medical Imaging, Helmholtz Zentrum München (GmbH), 85764 Neuherberg, Germany (e-mail: christian.zakian@helmholtz-muenchen.de).

Digital Object Identifier 10.1109/TMI.2021.3084356

I. Introduction

UNDERSTANDING organismal growth and development, as well as analyzing physiology and disease in intact tissues requires imaging tools that can penetrate deeper than optical microscopy. While optical microscopy is limited to depths of a few hundred micrometers due to photon scatter in tissue [1], optoacoustic imaging can go beyond the depth limit set by diffusion. Optoacoustics achieve improved depth when generating images based on acoustic wave propagation (acoustic diffraction), i.e. wave propagation that experiences 10^2- to 10^3-fold less scattering in tissues compared to light. Raster scan optoacoustic mesoscopy (RSOM), for example, provides up to sub-10 micron resolution of tissues within several millimetres depth [2], [3]. RSOM has found several applications in pre-clinical and clinical imaging. For example, it has been used to image model organisms [4], angiogenesis in tumor development [5], [6], and skin vasculature in healthy individuals and those with skin conditions [7].

RSOM collects data by scanning an ultrasound transducer over a sample and acquiring a projection at each scanning position. Here, "projection" refers to a depth-resolved, time-sampled optoacoustic signal (A-scan) over a volume, the latter being defined by the acceptance angle of the detector. Therefore, at each time point the detector measures the response from a spherical shell rather than from a single point in space. Three-dimensional RSOM images are reconstructed from a large amount of data, which can be as much as 1.35 GB uncompressed single precision for a 3D matrix containing $135 \times 1600 \times 1600$ data points. This number of data points would typically cover an area of $3.6mm \times 10mm \times 10mm$ and involve $10^7 - 10^8$ projections. Image reconstructions based on such data sets require significant computation. Typical RSOM inversion is based on backprojection or time-reversal methods [8]–[13]. Time-domain image reconstruction for the 3D matrix described above, containing $135 \times 1600 \times 1600$ data points, can take up to 1 hour with a quad-core processor @ 4 GHz. Model-based algorithms have also been tested and may yield better image quality, but generally have even higher computational burdens and memory requirements than back-projection [14], [15]. It would be beneficial to consider faster reconstruction algorithms to enable rapid, and possibly on-the-fly, reconstruction upon completion of scanning. This would support the promising use of RSOM for high-throughput imaging while maintaining good reconstruction quality.

Methods for 2D or 3D reconstructions of photoacoustic signals in the Frequency Domain have been suggested using the $\omega - k$ algorithm [16]–[19]. This algorithm relies on the technique of Stolt migration of ultrasound waves back to its source in the $\omega - k$ domain [20]. The $\omega - k$ algorithm has been employed in various areas such as radar imaging, ultrasound, and seismic imaging applications [21]–[23]. However, frequency domain inversions have not been widely considered in optoacoustic imaging, outside of a few demonstrations with simulated and *ex vivo* data [16]–[19]. These *ex vivo* preliminary studies have been followed by investigations on interpolation schemes for data conversion from a non-uniform to a uniform sampling grids, or on applications of non-uniform Fast Fourier Transform and zero-padding approaches to reduce artefacts in the final reconstructed image [24]–[27]. Nevertheless, to the best of our knowledge, the $\omega - k$ algorithm has never been applied to reconstruct *in vivo* optoacoustic data, has not been shown to yield the high image quality reached with time-domain inversions, nor has its performance been quantitatively compared in terms of speed and reconstruction quality with time-domain backprojection.

We postulated that frequency-domain inversion could become the driving scheme for optoacoustic image reconstruction, because it can provide an accelerated tomographic inversion over its time domain counterpart, resulting in high quality image generation with real-time processing. We focused on the inversion problem in raster-scan optoacoustic mesoscopy (RSOM) and aimed for a novel implementation of the $\omega - k$ algorithm, namely fast weighted $\omega - k$ (FWOK), with improved image quality by integrating the transfer function (impulse response) of the detector, while capitalizing on the computational speed of the Fourier domain. Frequency domain correction of the transfer function is computationally more efficient compared to time-domain approaches based on deconvolution [29]. Therefore, seamless correction of the sensitivity field of the detector can be achieved in the frequency domain by weighting the inversion with the transfer function (TF) of the detector [30]. We investigated the image quality achieved using the proposed fast weighted $\omega - k$ (FWOK) algorithm on data collected from phantoms and *in vivo*, and compared its imaging performance and reconstruction speed to the time-domain backprojection algorithm. We show that our proposed $\omega - k$ algorithm can achieve more than two orders of magnitude faster reconstruction speeds (360-fold increase) than time-domain inversions. The results point to frequency domain inversion as a highly advantageous approach for RSOM imaging due to superior reconstruction quality and speed demonstrated over time-domain reconstruction.

II. Methods

Section A describes the data acquisition for RSOM, and the 3D image reconstruction problem definition in terms of time-domain backprojection algorithm. Section B formulates and describes the reconstruction problem in terms of conventional frequency-domain space, namely the ω k algorithm. Section C describes the experimental setup used to generate the RSOM scans in this work. Section D describes the methodology for measuring the spatial sensitivity field of the transducer employed, necessary to obtain the detector transfer function of the system for correction in the fast weighted ω k algorithm (FWOK). Finally, section E introduces our proposed FWOK algorithm, which swiftly and with minimal computation cost embeds the spatial sensitivity correction of the transducer in the reconstruction process.

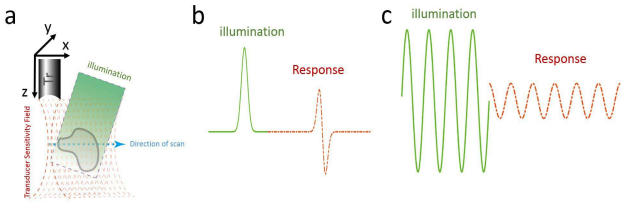

Fig. 1. RSOM scanning mechanism. For simplicity, only a single B-Scan is shown. Multiple B-scans are measured along the y direction. (a) Scanning setup (Tr: transducer.). (b) Schematic depicting illumination and transducer response in time-domain optoacoustics. (c) Schematic depicting illumination and transducer response in frequency-domain optoacoustics. A: amplitude t: time.

A. RSOM Data Acquisition and Backprojection in the Time-Domain

RSOM data are collected in a raster scan configuration [31] (**Figure 1a**). RSOM uses a focused transducer, whereby the focal point of the RSOM detector is considered to be a point unfocused detector, also termed the "virtual detector" [3], [10]. In the time-domain (TD), a time series data is collected at every (x_i, y_j) position (**Figure 1b**), in response to a nanoseconds-width light pulse excitation [30]. The scanning step size is ds along both the x-axis and y-axis, and the signal is digitized along the time axis with a time step dt. This acquisition can be also performed in the frequency domain by collecting data at discrete frequencies in response to modulated light excitation at multiple frequencies (**Figure 1c**) [32], [33]. The time- and frequency-domain measurements are equivalent and interchangeable via the one-dimensional Fourier transform. Nevertheless, here we consider the more common time-domain data collection scheme. Upon the completion of the measurement, the sampled signals are stored in a three-dimensional array $s(x, y, z = 0, t)$, where $z = 0$ signifies the scanning plane. The dimensions of the array are N_x, N_y, N_t in the dimensions x, y and t respectively. Even though the signal collected is in a discrete form, for simplicity, the algorithms in Sections B and E are presented in continuous-time formulation.

For TD reconstruction, we used an exact time-domain backprojection algorithm for the planar geometry, namely, the universal backprojection algorithm [8]. The algorithm was implemented with a fixed speed of sound. Backprojection reconstructs the image in 3D by projecting each received signal backward onto a spherical surface bounded by the transducer field of view.

B. RSOM Image Reconstruction Using the Conventional ω-k Algorithm

The goal of the reconstruction is to determine the light absorption map, which is equivalent to the initial pressure

$s(x, y, z, t = 0)$ that gives rise to the ultrasound waves collected at the scanning plane $z = 0$, i.e. $s(x, y, z = 0, t)$. We first perform a Fourier transform along the spatial dimensions x, y and the temporal dimension t of the raw data acquired at the scanning plane s $(x, y, z = 0, t)$ to obtain $S\left(k_x, k_y, z = 0, \omega\right)$ as

$$S\left(k_x, k_y, z = 0, \omega\right) = \int\int\int e^{-(ik_x x + ik_y y - i\omega t)} s\left(x, y, z = 0, t\right) dx dy dt, \quad (1)$$

where k_x and k_y correspond to the spatial frequencies in x and y dimensions (in m^{-1}) and ω is the temporal frequency (in rad/sec). After performing wavefield extrapolation [34] we can derive S at a certain depth z (i.e. the image depth)

$$S\left(k_x, k_y, z, \omega\right) = e^{ik_z z} S\left(k_x, k_y, z = 0, \omega\right). \quad (2)$$

Taking the inverse Fourier transform results in

$$s\left(x, y, z, t\right) = \int\int\int e^{ik_x x + ik_y y + ik_z z - i\omega t} S\left(k_x, k_y, 0, \omega\right) dk_x dk_y d\omega. \quad (3)$$

At $t = 0$, **Equation (3)** becomes

$$s\left(x, y, z, 0\right) = \int\int\int e^{ik_x x + ik_y y + ik_z z} S\left(k_x, k_y, 0, \omega\right) dk_x dk_y d\omega, \quad (4)$$

which describes the desired initial pressure. **Equation (4)** gives us the needed reconstruction of the image s but it poses two challenges. First, it has to be calculated for each z, which is computationally cumbersome. Second, it cannot be solved by the Fast Fourier Transform algorithm (FFT) due to the absence of the Fourier kernel of ω, which falls out of **Equation (2)** when $t = 0$.

We proceed to change the variables from ω to k_z in **Equation (4)** using the dispersion relation shown in **Equation (5)** which allows then to solve the equation using a 3D Fourier transform [20] and therefore use FFT. This variable change transfers the data from $\omega - k$ space to pure k-space. Using the dispersion relation [34], the temporal frequency can be expressed as

$$\omega = c\sqrt{k_x^2 + k_y^2 + k_z^2}, \quad (5)$$

where c is the speed of sound, assumed to be constant throughout the sample being measured. As the detected ultrasound waves in an RSOM scan propagate from the imaged object to the detector, i.e. opposite to the assumed herein direction of detection, we presumed that ω and k_z have opposite signs [35]. Therefore, the frequency can be written as

$$\omega = -sign\left(k_z\right) c\sqrt{k_x^2 + k_y^2 + k_z^2}. \quad (6)$$

Using **Equation (6)** to perform the change of variables in **Equation (4)**, we obtain

$$s\left(x, y, z\right) = \int\int\int S\left(k_x, k_y, 0, \omega\left(k_x, k_y, k_z\right)\right) \times J e^{ik_x x + ik_y y + ik_z z} dk_x dk_y dk_z, \quad (7)$$

where J is the variable-change Jacobian, i.e. so that $d\omega = J \cdot dk_z$ [36], and is defined as:

$$J = \frac{ck_z}{\sqrt{k_x^2 + k_y^2 + k_z^2}} \quad (8)$$

Since the dispersion relation between ω and k_z is nonlinear (see **Equation (6)**) the change of variables leads to an unequally spaced grid along k_z. Hence, an interpolation is needed to calculate k_z at a regular grid suitable for the inverse Fourier transform in the discretized form. (depicts the 2D results of a non $-$ linear transformation of a grid of 12×6 values generated for an arbitrary value of k_z.

C. The Experimental Setup

A high power laser diode (NDB7K75, Nichia, Anan, Japan) operating at 445 nm was used for scanning. The laser diode was driven using a high-current, short-pulse circuit [37]. Following the trigger signal from a function generator (33522B; Keysight, Santa Rosa, USA), this system provided a laser pulse with a duration of 7 ns. High voltage was applied using an adjustable high voltage supply (EA-3050B; EA, Viersen, Germany). Light emitted by the laser diode was coupled to a multimode glass fiber using a lens system, assembled from components provided by Thorlabs (Ann Arbor, USA). The fiber diameter was 200 μm with a numerical aperture (NA) of 0.22, leading into a 4×4 fiber coupler (MPC-4-M21-M41-P23; Lasfiberio, Xi'an, China), featuring four output fibers, each with a diameter of 200 μm and NA of 0.22. The outputs of these fibers were terminated with 1.25 mm ferrules and arranged circularly around the transducer, illuminating the transducer focal zone.

The transducer was spherically focused and had a 50 MHz central frequency, 112% relative bandwidth, 3 mm focal length and 0.5 NA (SNX140517_HFM23; Sonaxis, Besancon, France). The holder was constructed using a lithographic 3D printer (Formlabs, Somerville, USA).

The transducer and the fiber optics were placed on a XY stage (U-723; Physik Instrumente, Germany) and controlled by a dual-channel driver (C-867.260; Physik Instrumente, Karlsruhe, Germany). The signal from the transducer was fed into a 60-dB gain amplifier (AU-1291-R; Miteq, Hauppauge, USA) and finally digitized with 12-bit resolution at 200 Ms/s (Razor Express 14×2 CompuScope; Dynamic Signals LLC, Lockport, USA). The digitized data were stored on a solid-state drive (850 EVO Retail MZ-75E250B/EU; Samsung, Suwon, South Korea) for further processing. The entire system was controlled using a custom-designed MATLAB application (Mathworks, Natick, USA).

D. Measurement of the Transducer Spatial Impulse Response

In order to study whether we could account for the RSOM detector response during frequency domain image reconstruction, we determined the spatial transfer function of the transducer. The spatial transfer function is the frequency domain equivalent of the spatial impulse response,

a function that incorporates the electrical impulse response and the spatial sensitivity field of the transducer, the latter determined by the geometrical characteristics of the transducer. Besides correcting for the spatial response of the RSOM detector, capturing the spatial sensitivity also considers the effects that come from the assumption that RSOM uses a point detector, whereby the true detection area is determined by the finite focal point size achieved by the RSOM transducer [38]. Accounting for the effects of the spatial impulse response of the detector on the reconstructed image has been previously considered in the time-domain [30]; however, we were particularly interested in interrogating herein the equivalent implementation of this correction scheme in the frequency domain.

To determine the spatial transfer function (*STF*) of the detector employed, we scanned a ∼10 μm-diameter black polyethylene microsphere (BKPMS-1.2 10-20 μm, Cospheric LLC, USA) within the detector's field of view. The microsphere was placed at the same average depth (relative to the detector) as potential imaging targets to achieve optimal correction. The raw optoacoustic signal, M, acquired at the x-y scanning plane (z = 0) for the microsphere has the form $M(x, y, z = 0, t)$. Ideally, the microspheres serve as objects with dimensions that are smaller than the system's acoustic resolution. However, we opted for diameters closer to the resolution limit of RSOM (a few tens of microns) in order to obtain measurements with sufficient signal-to-noise ratio. The scanning step size was set to be smaller than half the system resolution to satisfy the Nyquist criterion [39]. The *STF* was then obtained by reconstructing M using the $\omega - k$ algorithm as described in Section II.B. The inverse FFT of the *STF* would provide the time domain-equivalent point spread function, *PSF*. However, this step is never performed, as our correction is done in the frequency domain. Finally, the *STF* was interpolated to match the grid of the RSOM scan to be corrected and applied as described in the next Section.

E. The Proposed FWOK Algorithm

The proposed FWOK algorithm uses the standard $\omega - k$ algorithm described in Section II.B as a backbone and incorporates the detector spatial sensitivity response in the frequency domain, offering both a faster and more accurate inversion scheme than time domain or standard $\omega - k$ alone. The detector spatial sensitivity is modelled by its Spatial Transfer Function $STF(k_x, k_y, k_z)$, which is defined as the Fourier transform of its spatial sensitivity, i.e. the spatial impulse response [30].

The algorithm builds upon the methodology presented in Section II.B. The frequency domain reconstructed data are stored in the form $S(k_x, k_y, k_z) = \hat{S} \times STF$, which allows a straightforward incorporation of the STF, by multiplying the data by the conjugate of the STF. The reconstructed data $\hat{S}$ is obtained by further multiplying the frequency domain reconstructed data by $1/|STF|^2$ to cancel out the correction process residual. Moreover, the noise variance σ_n^2 is added to prevent the right term of **Equation (9)** from diverging to infinity in the case of low signal-to-noise ratio [30], i.e.

$$\hat{S}(k_x, k_y, k_z) = S(k_x, k_y, k_z) \times \frac{STF^*(k_x, k_y, k_z)}{|STF|^2 + \sigma_n^2}, \quad (9)$$

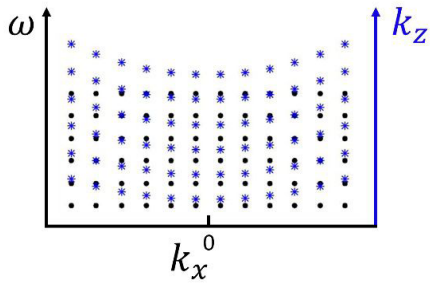

Fig. 2. 2D demonstration of the non-linear grid transformation effect of the variable change of **Equation. (4)**.

where σ_n^2 is the noise variance of the measured *STF* [40], which can be computed or found empirically.

Applying **Equation (9)** to the reconstructed signal S achieves three goals [30]. First, it accounts for any irregularity of the detector's sensitivity field. Therefore, multiplying the frequency domain signal S with the *STF* conjugate normalizes S to the detector sensitivity. Second, it corrects aberrations in the phase of the signal caused by undesirable acoustic reflections within the transducer. Third, it incorporates effects of the electric impulse response of the detector since the frequency response of the detector is also encoded in the sensitivity measurement of the detector.

Inversion of $\hat{S}$ in **Equation (9)** via the inverse Fourier transform produces a reconstructed image that is corrected for the spatial transfer function of the system employed. The algorithm is summarized in **Table I**.

For the purpose of simplicity, **Figure 3** shows the steps of the FWOK reconstruction process using a B-scan of two point sources. The initial raw optoacoustic signal in time-domain is displayed along the scanning direction x as an image in **Figure 3a**. A two-dimensional FFT operation is next applied to the raw data and shown in **Figure 3b**, with k_x as the spatial frequency axis along the scanning direction and ω as the temporal frequency axis. As described in Section II.B and indicated in **Figure 2**, a non-linear change of variable is required to map the temporal frequency to an equivalent spatial frequency k_z. **Figure 3c** shows the resulting image reconstructed after a change of variable (ω to k_z), and interpolated it into a uniform grid suitable for application to an inverse FFT at a later stage. **Figure 3d** shows the reconstructed data in **Figure 3c** after fast weighting using the STF of the system, which was previously acquired in Section II.D. Finally, applying a 2D inverse Fourier transform to the image in **Figure 3d** results in the reconstructed data in spatial coordinates ($x - z$) as shown in **Figure 3e**. For *in vivo* imaging, images were further processed by applying a 3D Hessian-based vesselness filter [41]. However, all quality assessment metrics presented below were performed on the reconstructed images before filtering.

F. Phantom and in Vivo Measurements

To evaluate the performance of the FWOK algorithm we investigated the image reconstruction quality using a contrast-to-noise metric described in the next section. We obtained optoacoustic data from a simple phantom comprising two 10 μm-diameter black surgical sutures placed parallel to the

TABLE I
THE PROPOSED FWOK ALGORITHM

Table I. The proposed FWOK algorithm

Input: Three dimensional signal acquired at z=0, $s(x, y, z = 0, t)$.
Output: 3D back-projected signal, $s(x, y, z, t = 0)$.

			Dimensions of Output Matrices
1.	Data Acquisition.	$s(x, y, z = 0, t)$	(N_x, N_y, N_t)
2.	3D Fast Fourier Transform.	FFT(s) → $S(k_x, k_y, \omega)$	$(N_x, N_y, N_\omega = N_t)$
3.	Retain positive frequencies.	$S(k_x, k_y, \omega > 0)$ → S	$(N_x, N_y, \frac{N_\omega}{2} - 1)$
4.	Filter the transducer BW.	$S(k_x, k_y, \omega_{max} > \omega > \omega_{min})$ → S	(N_x, N_y, N_ω^*), $N_\omega^* < \frac{N_\omega}{2} - 1$
5.	Signal propagation from focal point to the actual detector.	$Se^{-i\omega t_d}$ → S , t_d: time travel to the focal point.	(N_x, N_y, N_ω^*)
6.	Variable change from ω to k_z.	$S(k_x, k_y, \omega)$ → $S(k_x, k_y, k_z^*)$	$(N_x, N_y, N_z = N_\omega)$
7.	Interpolate from irregular to regular grid in k_z.	$S(k_x, k_y, k_z^*)$ → $S(k_x, k_y, k_z)$	(N_x, N_y, N_z)
8.	Generate the TF.	$FFT(PSF(x, y, z))$ → $STF(k_x, k_y, k_z)$	(N_x, N_y, N_z)
9.	Account for the TF.	$S(k_x, k_y, k_z) \times \frac{STF^*(k_z, k_x, k_y)}{\lvert STF\rvert^2 + \sigma_n^2}$ → S	(N_x, N_y, N_z)
10.	Back to the spatial domain by 3D IFFT.	$IFFT(S(k_x, k_y, k_z))$ → $s(x, y, z, t = 0)$	$(N_x, N_y, N_z^* = 2N_z)$

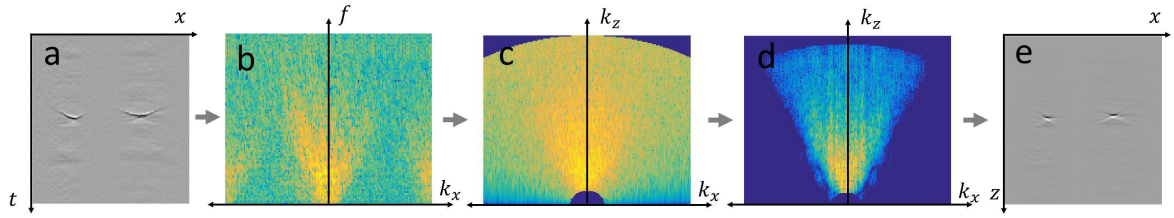

Fig. 3. An example of a 2D-reconstruction of an RSOM B-scan using the FWOK framework. a) Initial raw optoacoustic image of two black polyethylene microspheres, acting as point sources, in time-domain. Microspheres were approximately 10-20 μm in diameter. b) The positive portion of the frequency spectrum obtained by applying a two-dimensional FFT to the raw data, with k_x as the spatial frequency axis along the scanning direction and ω as the temporal frequency axis. Data is shown for frequencies within the transducer bandwidth. c) Resulting image reconstructed frequency spectrum after a change of variable (ω to k_z) and interpolation into a uniform grid. d) Reconstructed image frequency spectrum after applying STF system correction. e) Final step involving a 2D inverse Fourier transform of the image in d, resulting in the reconstructed data in spatial coordinates ($x - z$). Color dynamic ranges in b-c are unified.

imaging plane and crossing each other. The sutures were fixed in 1.5% agarose to prevent them from moving as the transducer was scanned. Our approach was compared to standard time domain and $\omega - k$ reconstruction approaches.

Next, we assessed the efficacy at reconstructing more complex and biologically-relevant structures, by applying the FWOK algorithm to images obtained from an *in vivo* mouse ear scan. A healthy adult CD-1 albino mouse (Envigo, Germany) was anesthetized using 1.8% gas isoflurane while breathing 100% O_2 and the ear gently placed against a supporting surface and coupled with acoustic gel for scanning. All procedures with animals were approved by the Government of Upper Bavaria.

G. Quality Assessment Metric

To quantify the image quality after reconstruction using the different algorithms, we selected three regions of interest (ROIs) from each image for representative areas containing the signal, background, and noise levels. More specifically, the region labelled "signal" comprised the entire optoacoustic measurement of the imaged structure, either the suture or the mouse ear vasculature. The region labelled "background" comprised the area surrounding the structure, which typically includes the signal spread that causes blurriness and loss of resolution due to the non-ideal nature of the imaging system and numerical errors introduced by the reconstruction computation. Finally, the area labelled "noise" comprised a region that was far from the sample, and represents the "dark noise" of the measurement. We used these regions to calculate the contrast-to-noise ratio (CNR) of the image for a case with non-zero mean noise, using the following equation:

$$CNR = \frac{\mu_S - \mu_B}{\mu_n + \sigma_n}, \tag{10}$$

where μ_s, μ_B and μ_n represent the average pixel values from the selected signal, background and noise ROIs, respectively, and σ_n represents the standard deviation of the pixel values within the noise ROI. CNR in **Equation (10)** was chosen as the quantitative quality indicator for our study as it reports specifically on the contrast gain achieved by the signal spread suppression when applying *STF* correction, and the image

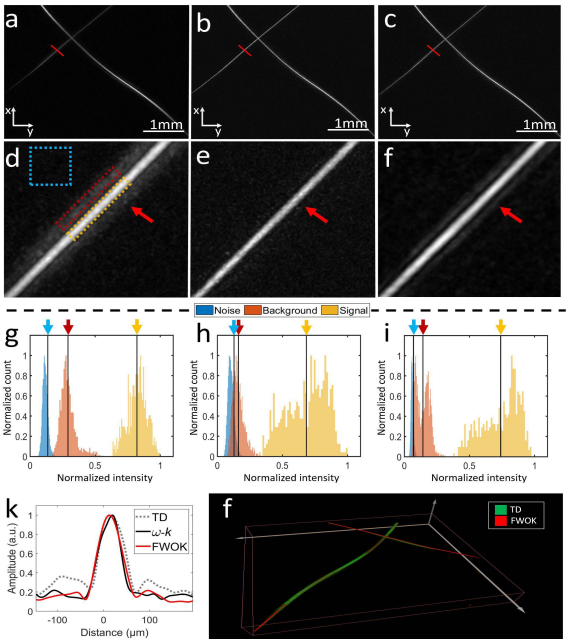

Fig. 4. Comparison of time-domain back-projection $\omega - k$ algorithm, and FWOK algorithms using phantom experiments. (a) Time-domain back-projection. (b) $\omega - k$. (c) FWOK. (d-f) Magnified views (7X) of panels (a)-(c), respectively. Red arrows in panels (d)-(f) point to possible reconstruction artefacts around the suture. Blue, red, and yellow dashed squares refer to the selected ROI of noise, background and signal, respectively, that are chosen to estimate CNR in Equation (10). (g-i) Normalized histogram of the selected ROIs in (d)-(f), respectively. Red and yellow arrows point to the mean of background and signal, respectively. Blue arrow points to the sum of the mean and standard deviation of the noise. (k) Normalized intensity profile across the red lines in panels (a)-(c). (f) 3D visualization of the reconstruction in panels (a) and (c), overlaid on top of each other.

noise floor propagation resulting from each reconstruction method.

III. Results

A primary motivation of the experimental work was to investigate the image quality achieved by frequency domain inversion compared to the time-domain inversion, the latter considered in this study as the gold standard in image quality. We sought to capitalize on the inversion speed gains in the frequency domain to obtain processed images faster than is possible in the time-domain, while still increasing the image quality by incorporating the impulse response correction of the system within Fourier reconstruction framework.

To compare the *CNR* and lateral resolutions obtained when reconstructing the optoacoustic volumetric data using the time-domain, $\omega - k$, and FWOK approaches, we imaged a simple suture target with a known thickness. **Figures 4a-c** show a large field of view reconstructed for the cross-suture arrangement embedded in agar, using the time-domain backprojection (**Figure 4a**), conventional $\omega - k$ (**Figure 4b**), and our proposed FWOK algorithms (**Figure 4c**). A sub-region of the complete field-of-view was further inspected for finer quality assessment and 7X-magnifications shown for the corresponding cases in **Figures 4d-f**, respectively. To proceed with the quality quantification, we defined the regions of interest depicted in **Figure 4d** for areas containing the signal (yellow border), the background (red border), and the noise (blue border). The same selected regions of interest were applied to all three reconstructed image cases for consistency. Histograms of the pixel value enclosed by each region of interest were generated to visualize the contrast level reflected by **Equation (10)**. To enable a comparative visualization of the relative mean separation and standard deviation of each pixel value distribution, we first normalized the corresponding reconstructed image to the maximum pixel value within the three regions combined, and then normalized the histogram obtained for each region to its maximum count, thereby adjusting for the different areas enclosed by each region. **Figure 4g-i** show the normalized ROI histograms for the time-domain backprojection (**Figure 4g**), conventional $\omega - k$ (**Figure 4h**), and FWOK (**Figure 4i**) reconstructed images. The red and yellow vertical arrows in the histograms indicate the position of the signal (yellow) and background (red) mean values, respectively. The blue arrow indicates the value positions for the mean plus one standard deviation of the noise, which is necessary to account for a non-zero mean noise value as reflected by the denominator in **Equation (10)**.

The quality indices obtained for each method were: $CNR = 3.88$ for conventional backprojection, $CNR = 4$ for the $\omega - k$ algorithm, and $CNR = 8.5$ for the proposed FWOK algorithm. Artefacts were further reduced in the reconstruction by incorporating the transfer function-based weighting step into the FWOK algorithm, leading to background suppression around the suture. FWOK leads to a greater separation between mean signal values from the suture and mean background values around the suture and a concomitant reduction in the noise level, yielding a 2-fold improvement in CNR for FWOK compared to conventional $\omega - k$ and time-domain algorithms.

The similarity in *CNR* between time-domain and conventional $\omega - k$ algorithms is expected, as these result from equivalent mathematical calculations in two domains, which confirms that *CNR* improvement is primarily a result of the impulse response introduced in our reconstruction algorithm. Moreover, this implies that our approach could enhance the sensitivity of the system by suppressing noise levels. To evaluate the effect of *CNR* on image resolution we analyzed line intensity profiles along the suture for each method of reconstruction (**Figures 4a-c**, red lines). To enable a direct comparison of the resolution independently of the images dynamic range, we normalized each line profile by its maximum and show the results in **Figure 4k**. By calculating the full width half maximum of each line profile, we find that resolutions were 71 μm in the case of time-domain backprojection, and 56 μm for both, the conventional $\omega - k$ and FWOK algorithms. These results indicate that the $\omega - k$ algorithm alone allows an approximately 26% improvement in image resolution, independent of the additional weighting step in the FWOK algorithm.

To visualize the agreement of the volumetric optoacoustic reconstructed information obtained with time-domain and FWOK algorithms, we rendered the field-of-view in three dimensions, overlaying the results of both the time-domain and FWOK approaches (**Figure 4f**). We observe that the FWOK reconstruction (shown in red) resolves the entire cross-suture arrangement, while the time-domain reconstruction results in a

lower resolution image with the suture appearing thicker in the corresponding green overlay, in agreement with the resolution assessment described above.

To investigate the associated computational costs, we analysed the processing time for FWOK and standard time-domain reconstructions. We found that time-domain backprojection reconstruction calculations required over 1 hour of computation time to generate the image shown in **Figure 4a**; in contrast, the same image required only 10 seconds to be reconstructed with the FWOK algorithm (**Figure 4c**) using the same computer processing power. Importantly, while the detector transfer function correction in FWOK involves a simple and fast matrix division, an analogous step in the time-domain would require a time-consuming deconvolution operation. Time-domain deconvolution could also improve image quality in a similar manner to FWOK; however, this would add a significant computation time, further slowing the reconstruction. Therefore, introducing the impulse response correction in the frequency domain, as proposed herein, is an important step towards enabling real-time and high-quality optoacoustic reconstruction.

To evaluate the performance of our reconstruction approach in samples with higher structural complexity and biological relevance, we acquired *in vivo* optoacoustic images of mouse ear vasculature. **Figures 5a-c** show the reconstructed images of the mouse ear data using time-domain backprojection (**Figure 5a**), conventional $\omega - k$ (**Figure 5b**), and FWOK algorithms (**Figure 5c**). **Figures 5d-f** show 2X-magnifications of the images in **Figures 5a-c** to highlight fine differences afforded by the respective reconstruction approaches. Two examples of the superior performance of our FWOK reconstruction are indicated by the white arrows in **Figures 5d-f**. The first example (**i**) consists of two vessels that are easily resolved in our FWOK reconstruction (**Figure 5f**), but blur together in the time-domain backprojection reconstruction (**Figure 5d**). The second case (**ii**) is a vessel that is clearly retrieved with our FWOK approach (**Figure 5f**) but is instead merged and lost into the background for the time-domain backprojection (**Figure 5d**). The resolution enhancement is quantitatively confirmed by the full width half maximum values obtained for a line profile across a representative vessel, which is indicated by the white line in **Figures 4a-c**. The line profiles are plotted for each reconstruction method in **Figure 5g**. We find a FWHM value of 74 μm for the line profiles coming from both the FWOK and standard $\omega - k$ reconstructed images, compared to a 103 μm obtained from the time-domain backprojection. This is in agreement with the measurements performed with the simple suture phantom above, resulting in a 25% increase in resolution using the frequency-based approaches.

We further calculated the *CNRs* for the FWOK (**Figures 5c**) and time-domain reconstructions (**Figure 5a**) to be 7 and 3, respectively. These values agree with the doubling in *CNR* observed for the suture phantom (**Figure 4**). Therefore, FWOK significantly improved the overall image quality of a complex three-dimensional vascular networks, producing sharper vessel structures and revealing a higher definition vascular architecture than with the alternative methods. This can be further appreciated in the volumetric images displayed in **Figures 5h** and **5i** for time-domain and FWOK reconstructions, respectively.

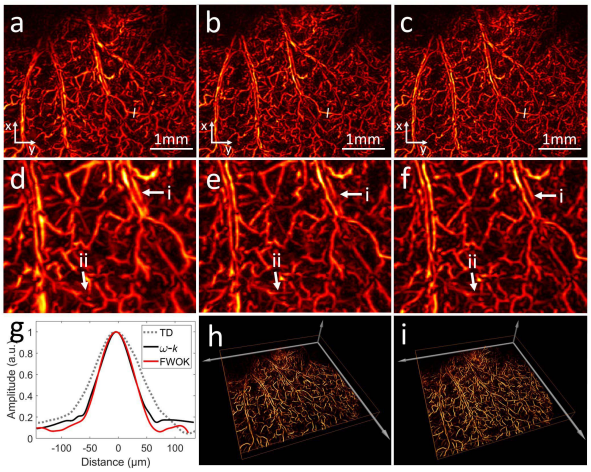

Fig. 5. Comparison of in vivo images of mouse ear vasculature using different reconstruction methods. (a-c) Top-view maximum intensity projections (MIP) of the reconstructions performed using (a) time-domain backprojection, (b) $\omega - k$ algorithm, and (c) FWOK algorithm. (d-f) Respective magnified views (2X) of panels (a)-(c). White arrows point to substantial differences in quality among the reconstruction methods. (g) Normalized intensity profile across the white lines in panels (a)-(c). visualization of the reconstruction in panel (a). (i) 3D visualization of the reconstruction in panel (c).

We next analyzed the reconstruction times for the mouse ear vasculature data using each method in order to confirm the processing speed acceleration resulting from using the FWOK reconstruction on data from complex vascular structures. Notably, for the reconstruction of the *in vivo* images shown **Figure 5a-c** ($1000 \times 1000 \times 140$ voxels), the computation time was 30 minutes for the time-domain backprojection, but only 6 seconds for the same data set using the FWOK algorithm. This means that FWOK can reconstruct a single B-scan of 140×1000 pixels in 20 milliseconds compared to 8 seconds for the backprojection algorithm. This results in a 360-fold increase in reconstruction speed, for which weighting by the Transfer Function in the FWOK algorithm consumed only 15% more time than the traditional $\omega - k$ algorithm. FWOK offers high quality reconstruction at speeds that are over two-orders of magnitude faster than conventional time-domain methods, making it an attractive option for real-time processing for optoacoustic mesoscopy.

IV. Discussion

We introduced the FWOK inversion algorithm in optoacoustic imaging, which is an extension of the standard $\omega - k$ reconstruction inversion that incorporates the spatial impulse response of the physical system. We investigated the image reconstruction quality achieved using FWOK with *in vivo* RSOM data and compared its performance to both standard $\omega - k$ and time-domain back-projection inversions. FWOK capitalizes on the inversion speed of frequency domain [16] and the fast matrix division operation to include the impulse response function in this domain, thereby avoiding the lengthy deconvolution step required to perform the equivalent operation in the time domain [29]. FWOK enabled reconstruction

of RSOM images faster than in time-domain without compromising in reconstructed image *CNR* and resolution.

We showed that the proposed FWOK inversion could reconstruct a large optoacoustic data set (1000 × 1000 × 140 voxels) two orders of magnitude (360-fold) faster than time-domain backprojection, without compromising image quality. This accelerated processing time was enabled by FWOK's inherent block-processing of the entire dataset in one step, instead of the point-by-point computation in time-domain. The algorithm exploits the fast computational speed of FFT to reconstruct B-scans in fractions of a second to afford 3D images immediately after acquisition. Reconstruction speeds have been previously accelerated using standard frequency domain reconstruction with experimental optoacoustic data, with a 53 s-reconstruction time for a data size of 200 × 200 × 100 voxels in Fourier domain, compared to nearly 3 hours in time-domain based reconstruction for the same data set [27], representing a 200-fold faster reconstruction. Recently, Fourier reconstruction times of 0.25 s were reported for B scans with 600 × 751 pixels [42] and of 0.7 s for multi-layer volumetric reconstruction of a 40 × 40 × 2000 voxel-data set [43]. Here we achieve reconstruction times of 6 s for over 40 times larger data sizes than previously demonstrated. The faster performance obtained with our algorithm could be attributed to the use of single rather than double precision data formats, 2D instead of 1D interpolation in k-space which avoids unnecessary iterations, and a simplification to a single-layer instead of a multi-layer reconstruction approach.

We demonstrated that the FWOK inversion can compensate for the system's non-ideal response and enhance the *CNR* and resolution of the final reconstructed optoacoustic image compared to the standard $\omega - k$ algorithm and time-domain back-projection. This compensation was achieved by experimentally measuring the spatial transfer function and applying it as a multiplicative weighting function in the frequency domain inversion scheme of the acquired RSOM data. Although incorporating the *PSF* has been shown to successfully improve the quality of reconstructed optoacoustic images [30], [44], [45] and detector sensitivity fields have been included in reconstruction algorithms to account for negatively focused ultrasound transducers [46], [47], these studies were performed in the time-domain and suffered from long processing times. Here we incorporate the *PSF* correction factor in the reconstruction problem in the Fourier domain to avoid sacrificing computational time. Note, however, that each position in a defined 3D space has an associated temporal acoustic signal, resulting in a 4D function describing the complete transducer spatial response in the system [48]. Here we obtained the spatial transfer function at a single depth position, reducing it to a 3D function, and show that this simplification holds as a good approximation for locations relatively close to the depth position at which the *PSF* is measured.

Our findings show that FWOK results in background and noise reduction which enhances the contrast from the signal, resulting in higher *CNR* and resolution compared to both standard $\omega - k$ and time-domain back-projection. We validate our reconstruction approach on a simple suture phantom and more complex mouse ear vasculature with *in-vivo* data and find that reconstruction is accelerated and produces higher image quality and reduced background noise compared to standard $\omega - k$ and time-domain back-projection. We believe this to be the first *in-vivo* demonstration of frequency-domain reconstructions of RSOM images. Previous RSOM images of vascular networks have been processed in time domain at the cost of heavy reconstruction computation [49].

Reconstruction with the FWOK algorithm remains vulnerable to artefacts introduced by assuming a fixed speed of sound in the reconstruction algorithm and by the interpolation errors required to convert the data to a uniform grid suitable for inverse Fourier transform for image reconstruction (step c of **Figure 3**) [24], [25]. However, neglecting the speed of sound variation in soft tissues has been shown to have negligible effects on the image reconstruction quality due to small changes in speed around 1500 m/s within the full imaging volume [50]. Numerical errors during the interpolation step have been reduced by employing a Sinc interpolation function, yet this remains computationally expensive [51], [29]. Alternatively, non-equispaced grid sampling has been implemented to avoid the interpolation step in Fourier domain [27]; however, this results in a significant increase in computational complexity. In this work, we used a cubic spline interpolation as a compromise between quality and computational cost.

Frequency-domain implementations are challenged by the large random access memory (RAM) required to perform the calculation. Whereas time-domain reconstruction inversions are performed point-by-point, frequency-domain inversions significantly accelerates the reconstruction time by computing the full inversion in one step, in exchange for an increase in the memory demand. For instance, the *in-vivo* image presented in **Figure 5** required 8 GB of RAM to reconstruct an optoacoustic dataset size of 1 GB. Future work will examine strategies to further improve memory use efficiency.

In summary, FWOK provides faster computation than time-domain backprojection while directly incorporating the spatial transfer function in the frequency domain enhancing *CNR* and resolution across the entire reconstructed image. These findings show that frequency domain inversions could become the method of choice for RSOM, significantly accelerating image reconstruction without compromising quality. We are expanding these efforts to incorporate FWOK for real time acquisition, processing and display of RSOM images and further expand the application of the algorithm into other scanning geometries, such as for optoacoustic tomography, where it could also provide high-performance reconstructions for real-time clinical applications.

ACKNOWLEDGMENT

The authors would like to thank Dr. Robert Wilson and Dr. Chapin Rodriguez for their support in refining the manuscript. They would also like to thank Dr. Juan Aguirre for his intellectual support in this study.

REFERENCES

[1] V. Ntziachristos, "Going deeper than microscopy: The optical imaging frontier in biology," *Nature Methods*, vol. 7, no. 8, pp. 603–614, Aug. 2010.

[2] M. Omar, J. Gateau, and V. Ntziachristos, "Raster-scan optoacoustic mesoscopy in the 25-125 MHz range," *Opt. Lett.*, vol. 38, no. 14, pp. 2472–2474, Jul. 2013.

[3] M. Omar, J. Aguirre, and V. Ntziachristos, "Optoacoustic mesoscopy for biomedicine," *Nature Biomed. Eng.*, vol. 3, no. 5, pp. 354–370, May 2019, doi: 10.1038/s41551-019-0377-4.

[4] H.-C.-A. Lin *et al.*, "Selective plane illumination optical and optoacoustic microscopy for postembryonic imaging," *Laser Photon. Rev.*, vol. 9, no. 5, pp. L29–L34, Sep. 2015.

[5] M. Omar, M. Schwarz, D. Soliman, P. Symvoulidis, and V. Ntziachristos, "Pushing the optical imaging limits of cancer with multi-frequency-band raster-scan optoacoustic mesoscopy (RSOM)," *Neoplasia*, vol. 17, no. 2, pp. 208–214, Feb. 2015.

[6] C. J. H. Ho, *Frontiers in Biophotonics for Translational Medicine*. Cham, Switzerland: Springer, 2016, pp. 75–109.

[7] J. Aguirre *et al.*, "Precision assessment of label-free psoriasis biomarkers with ultra-broadband optoacoustic mesoscopy," *Nature Biomed. Eng.*, vol. 1, no. 5, p. 0068, May 2017.

[8] M. Xu and L. V. Wang, "Universal back-projection algorithm for photoacoustic computed tomography," *Phys. Rev. E, Stat. Phys. Plasmas Fluids Relat. Interdiscip. Top.*, vol. 71, no. 1, Jan. 2005, Art. no. 016706.

[9] A. Rosenthal, V. Ntziachristos, and D. Razansky, "Acoustic inversion in optoacoustic tomography: A review," *Current Med. Imag. Rev.*, vol. 9, no. 4, pp. 318–336, Jan. 2014.

[10] M.-L. Li, H. F. Zhang, K. Maslov, G. Stoica, and L. V. Wang, "Improved *in vivo* photoacoustic microscopy based on a virtual-detector concept," *Opt. Lett.*, vol. 31, pp. 474–476, Feb. 2006.

[11] Y. Xu and L. V. Wang, "Time reversal and its application to tomography with diffracting sources," *Phys. Rev. Lett.*, vol. 92, no. 3, Jan. 2004, Art. no. 033902.

[12] P. Beard, "Biomedical photoacoustic imaging," *Interface Focus*, vol. 1, no. 4, pp. 602–631, 2011.

[13] M. Mozaffarzadeh, A. Hariri, C. Moore, and J. V. Jokerst, "The double-stage delay-multiply-and-sum image reconstruction method improves imaging quality in a LED-based photoacoustic array scanner," *Photoacoustics*, vol. 12, pp. 22–29, Dec. 2018, doi: 10.1016/j.pacs.2018.09.001.

[14] J. Aguirre, A. Giannoula, T. Minagawa, L. Funk, P. Turon, and T. Durduran, "A low memory cost model based reconstruction algorithm exploiting translational symmetry for photoacoustic microscopy," *Biomed. Opt. Exp.*, vol. 4, pp. 2813–2827, Dec. 2013.

[15] M. A. Caballero, A. Rosenthal, J. Gateau, D. Razansky, and V. Ntziachristos, "Model-based optoacoustic imaging using focused detector scanning," *Opt. Lett.*, vol. 37, pp. 4080–4082, Oct. 2012.

[16] K. P. Köstli, M. Frenz, H. Bebie, and H. P. Weber, "Temporal backward projection of optoacoustic pressure transients using Fourier transform methods," *Phys. Med. Biol.*, vol. 46, no. 7, pp. 1863–1872, Jul. 2001, doi: 10.1088/0031-9155/46/7/309.

[17] R. Schulze *et al.*, "On the use of frequency-domain reconstruction algorithms for photoacoustic imaging," *J. Biomed. Opt.*, vol. 16, no. 8, 2011, Art. no. 086002.

[18] K. P. Kostli, D. Frauchiger, J. J. Niederhauser, G. Paltauf, H. P. Weber, and M. Frenz, "Optoacoustic imaging using a three-dimensional reconstruction algorithm," *IEEE J. Sel. Topics Quantum Electron.*, vol. 7, no. 6, pp. 918–923, Dec. 2001.

[19] B. E. Treeby and B. T. Cox, "K-wave: MATLAB toolbox for the simulation and reconstruction of photoacoustic wave fields," *J. Biomed. Opt.*, vol. 15, no. 2, 2010, Art. no. 021314, doi: 10.1117/1.3360308.

[20] R. H. Stolt, "Migration by Fourier transform," *Geophysics*, vol. 43, no. 1, pp. 23–48, Feb. 1978.

[21] L. Liang, M. Jungang, J. Yuesong, and L. Zhiping, "Near-field radar 3D synthetic aperture imaging based on Stolt interpolation," in *Proc. Asia–Pacific Microw. Conf. (APMC)*, 2005, p. 4.

[22] G. F. Margrave and M. P. Lamoureux, *Numerical Methods of Exploration Seismology: With Algorithms in MATLAB*. Cambridge, U.K.: Cambridge Univ. Press, 2019.

[23] M. H. Skjelvareid, T. Olofsson, Y. Birkelund, and Y. Larsen, "Synthetic aperture focusing of ultrasonic data from multilayered media using an omega-K algorithm," *IEEE Trans. Ultrason., Ferroelectr., Freq. Control*, vol. 58, no. 5, pp. 1037–1048, May 2011.

[24] W. Harlan, "Avoiding interpolation artifacts in Stolt migation," Stanford Explor. Project, Tech. Rep. 30, May 1982, pp. 103–110.

[25] J. Ronen, "Stolt migraton; interpolation artifacts," Stanford Explor. Project, Tech. Rep. 30, May 1982, pp. 95–102.

[26] Y. Xu, D. Feng, and L. V. Wang, "Exact frequency-domain reconstruction for thermoacoustic tomography. I. Planar geometry," *IEEE Trans. Med. Imag.*, vol. 21, no. 7, pp. 823–828, Jul. 2002.

[27] J. Schmid, T. Glatz, B. Zabihian, M. Liu, W. Drexler, and O. Scherzer, "Nonequispaced grid sampling in photoacoustics with a nonuniform fast Fourier transform," *J. Biomed. Opt.*, vol. 21, no. 1, Jan. 2016, Art. no. 015005, doi: 10.1117/1.JBO.21.1.015005.

[28] J. Kauppinen and J. Partanen, *Fourier Transforms in Spectroscopy*, 1st ed. Hoboken, NJ, USA: Wiley, 2001.

[29] J. B. Pawley, *Handbook of Biological Confocal Microscopy*, 3rd ed. Cham, Switzerland: Springer, 2006.

[30] M. Omar *et al.*, "Optical imaging of post-embryonic zebrafish using multi orientation raster scan optoacoustic mesoscopy," *Light, Sci. Appl.*, vol. 6, no. 1, Jan. 2017, Art. no. e16186, doi: 10.1038/lsa.2016.186.

[31] J. Aguirre, M. Schwarz, D. Soliman, A. Buehler, M. Omar, and V. Ntziachristos, "Broadband mesoscopic optoacoustic tomography reveals skin layers," *Opt. Lett.*, vol. 39, no. 21, pp. 6297–6300, Nov. 2014.

[32] P. Mohajerani, S. Kellnberger, and V. Ntziachristos, "Frequency domain optoacoustic tomography using amplitude and phase," *Photoacoustics*, vol. 2, no. 3, pp. 111–118, Sep. 2014.

[33] S. Kellnberger *et al.*, "Optoacoustic microscopy at multiple discrete frequencies," *Light, Sci. Appl.*, vol. 7, no. 1, p. 109, Dec. 2018, doi: 10.1038/s41377-018-0101-2.

[34] E. G. Williams, *Fourier Acoustics: Sound Radiation and Nearfield Acoustical Holography*. Amsterdam, The Netherlands: Elsevier, 1999.

[35] M. H. Skjelvareid, "Synthetic aperture ultrasound imaging with application to interior pipe inspection," M.S. thesis, Dept. Phys. Technol., Tromsø, Norway, 2012.

[36] L. Brand, *Advanced Calculus: An Introduction to Classical Analysis*. New York, NY, USA: Dover, 2013.

[37] A. Stylogiannis, L. Prade, A. Buehler, J. Aguirre, G. Sergiadis, and V. Ntziachristos, "Continuous wave laser diodes enable fast optoacoustic imaging," *Photoacoustics*, vol. 9, pp. 31–38, Mar. 2018, doi: 10.1016/j.pacs.2017.12.002.

[38] B. T. Cox and B. E. Treeby, "Effect of sensor directionality on photoacoustic imaging: A study using the k-wave toolbox," *Proc. SPIE*, vol. 7564, Feb. 2010, Art. no. 75640I, doi: 10.1117/12.841671.

[39] R. G. Lyons, *Understanding Digital Signal Processing*, 3rd ed. Upper Saddle River, NJ, USA: Prentice-Hall, 2011.

[40] L. P. Yaroslavsky and H. J. Caulfield, "Deconvolution of multiple images of the same object," *Appl. Opt.*, vol. 33, no. 11, pp. 2157–2162, Apr. 1994.

[41] A. F. Frangi, W. J. Niessen, K. L. Vincken, and M. A. Viergever, "Multiscale vessel enhancement filtering," in *Proc. Int. Conf. Med. Image Comput. Comput.-Assist. Intervent.* Cham, Switzerland: Springer, 1998, pp. 130–137.

[42] F. Spadin, M. Jaeger, R. Nuster, P. Subochev, and M. Frenz, "Quantitative comparison of frequency-domain and delay-and-sum optoacoustic image reconstruction including the effect of coherence factor weighting," *Photoacoustics*, vol. 17, Mar. 2020, Art. no. 100149, doi: 10.1016/j.pacs.2019.100149.

[43] H. Jin, S. Liu, R. Zhang, S. Liu, and Y. Zheng, "Frequency domain based virtual detector for heterogenous media in photoacoustic imaging," *IEEE Trans. Comput. Imag.*, vol. 6, Jan. 2020.

[44] K. B. Chowdhury, J. Prakash, A. Karlas, D. Justel, and V. Ntziachristos, "A synthetic total impulse response characterization method for correction of hand-held optoacoustic images," *IEEE Trans. Med. Imag.*, vol. 39, no. 10, pp. 3218–3230, Oct. 2020, doi: 10.1109/Tmi.2020.2989236.

[45] M. Seeger, "Pushing the boundaries of optoacoustic microscopy by total impulse response characterization," *Nature Commun.*, vol. 11, Jun. 2020, Art. no. 2910, doi: 10.1038/s41467-020-16565-2.

[46] G. Drozdov and A. Rosenthal, "Analysis of negatively focused ultrasound detectors in optoacoustic tomography," *IEEE Trans. Med. Imag.*, vol. 36, no. 1, pp. 301–309, Jan. 2017, doi: 10.1109/Tmi.2016.2606482.

[47] G. Drozdov, A. Levi, and A. Rosenthal, "The impulse response of negatively focused spherical ultrasound detectors and its effect on tomographic optoacoustic reconstruction," *IEEE Trans. Med. Imag.*, vol. 38, no. 10, pp. 2326–2337, Oct. 2019, doi: 10.1109/Tmi.2019.2897588.

[48] Z. Ali, C. Zakian, and V. Ntziachristos, "Ultra-broadband axicon transducer for optoacoustic endoscopy," *Sci. Rep.*, vol. 11, no. 1, Dec. 2021, Art. no. 1654, doi: 10.1038/s41598-021-81117-7.

[49] J. Aguirre *et al.*, "Precision assessment of label-free psoriasis biomarkers with ultra-broadband optoacoustic mesoscopy," *Nature Biomed. Eng.*, vol. 1, no. 5, pp. 1–8, 2017, doi: 10.1038/s41551-017-0068.

[50] M. O. Culjat, D. Goldenberg, P. Tewari, and R. S. Singh, "A review of tissue substitutes for ultrasound imaging," *Ultrasound Med. Biol.*, vol. 36, no. 6, pp. 861–873, Jun. 2010.

[51] V. Kober, M. Unser, and L. P. Yaroslavsky, "Spline and sinc signal interpolations in image geometrical transforms," *Proc. SPIE*, vol. 2363, pp. 152–161, Jan. 1995, doi: 10.1117/12.199628.